Understanding the Co-passivation Effect of Cl and Se for CdTe Grain Boundaries

Akash Shah,*,† Anthony P. Nicholson,† Thomas AM Fiducia,‡ Ali Abbas,‡ Ramesh Pandey,¶ Junliang Liu,§ Chris Grovenor,§ John M. Walls,‡ Walajabad S. Sampath,† and Amit H. Munshi†

†*Department of Mechanical Engineering, Colorado State University, Fort Collins, CO 80523, United States*

‡*CREST (Centre for Renewable Energy Systems Technology), Loughborough University, Leicestershire, LE11 3TU, United Kingdom*

¶*Department of Physics, Colorado State University, Fort Collins, CO 80523, United States*

§*Department of Materials, University of Oxford, United Kingdom*

E-mail: akash.shah@colostate.edu

Abstract

Chlorine passivation treatment of cadmium telluride (CdTe) solar cell improves device performance by assisting electron-hole carrier separation at CdTe grain boundaries. Further improvement in device efficiency is observed after alloying the CdTe absorber layer with selenium. High resolution secondary ion mass spectroscopy (Nano-SIMS) imaging has been used to determine the distribution of selenium and chlorine at the CdTe grain boundaries in a selenium-graded CdTe device. Atomistic modeling based on density functional theory (DFT-1/2) further reveals that the presence of selenium and chlorine at an exemplar (110)/(100) CdTe grain boundary passivates critical acceptor defects and leads to n-type inversion at the grain boundary. The defect state analysis provides an explanation for the band bending effects observed in the energy band alignment results, thereby elucidating mechanisms for high efficiencies observed in Se alloyed and Cl passivated CdTe solar cells.

Keywords: CdTe solar cells, Atomistic modeling, Defect passivation, Grain boundaries, Energy band alignment, Density Functional Theory, Electronic structure

Introduction

Cadmium telluride solar cells are a key technology in the photovoltaics (PV) market. The optimization of processing steps such as alloying selenium (Se) with the CdTe as well as replacement of contact and buffer layers have led to 22.1% efficient research scale CdTe device.[1–4] One of the important fabrication steps that has enhanced efficiency involves cadmium chloride ($CdCl_2$) treatment of the CdTe absorber layer. Published literature shows the $CdCl_2$ treatment of polycrystalline (px) CdTe based cells leads to superior device performance compared to single crystal CdTe based solar cell.[5] This suggests that the chlorine (Cl) interaction with the grain boundaries is crucial to obtain high efficiencies in px-CdTe solar cells.

Over the years, researchers have proposed several mechanisms to explain the success of $CdCl_2$ treatment in improving the CdTe device performance.[6] Numerous reports conclude that the high temperature $CdCl_2$ treatment of the CdTe layer leads to recrystallization and grain growth along the close packed (111) orientation.[7–9] It has also been proposed that $CdCl_2$ heat treatment passivates the deep defect levels and enhances the charge carriers lifetime.[6,10,11] In another report, *Li et al.* using scanning transmission electron microscopy along with density functional theory described that Cl substitution of the tellurium (Te) sites leads to n-type inversion at the grain boundary.[12] Therefore, a local p-n junction is established between the grain interior and the grain boundary which assists in separation of electron-hole pair charge carriers.

Along with $CdCl_2$ passivation treatment, recent device efficiency improvements to 22.1% have been realized by alloying Se within the CdTe film.[4] Published literature reveals, $CdCl_2$ treatment of Se alloyed CdTe layer leads to Se grading through the CdTe grain boundary, forming a graded $CdSe_xTe_{1\text{-}x}$/CdTe absorber layer.[13,14] One study shows that grading Se in the CdTe film passivates the non-radiative recombination centers in the bulk material.[13] It is also thought that the improvement in minority carrier lifetime is due to the presence of Se and Cl in the CdTe grain boundaries.[14] These findings emphasize the need to understand the effects of grading Se from $CdSe_xTe_{1\text{-}x}$ to CdTe absorber layers to further improve the device performance.

Several studies in past using experimental and theoretical techniques have explored the electronic properties of bulk $CdSe_xTe_{1\text{-}x}$.[15–18] However, the combined effects of Se and Cl at the CdTe grain boundaries on the electronic structure and charge carrier transport behaviors are unknown. In this work, we report the Se, Cl atomic scale composition and electronic structure of the grain boundaries through nano SIMS and density functional theory simulations respectively. The study demonstrates that alloying Se and Cl together at the grain boundary passivates deep level acceptor trap states when compared to bare (unalloyed) or only Cl at the CdTe grain boundary. The energy band alignment result shows high density of benign donor states existing below the Fermi level. The presence of high density benign donor states inverts the boundary region from p-type to n-type, establishing a local p-n junction for efficient charge extraction. This understanding of the role of Se and Cl in copassivating the CdTe grain boundary defect states provides useful details that can further contribute to higher CdTe device efficiency.

Results

CdTe and $CdSe_xTe_{1-x}$/CdTe absorber based PV devices

To perform the study, two CdTe cells (with and without Cl) and one CdSeTe/CdTe absorber based solar cells were fabricated as described in the methods section. Figure 1 (a) shows the schematic device structure of the CdSeTe/CdTe solar cell. To understand the effect of alloying selenium and chlorine on the device performance, the CdSeTe/CdTe film and one CdTe absorber based substrate received the $CdCl_2$ treatment while the other CdTe substrate was finished into device without any $CdCl_2$ treatment. The electrical measurements were performed on the finished devices to generate the current density vs voltage diode curves. The box plot (see Figure 2) depicts the Open-circuit Voltage (V_{OC}), Short-circuit current density (J_{SC}), Fill Factor (%), and Efficiency (η) comparison between the untreated CdTe, $CdCl_2$-treated CdTe and $CdCl_2$-treated CdSeTe/CdTe based PV devices. Comparing the device parameters from the box plot results (see Figure 2), it was evident that the $CdCl_2$ treatment of the CdTe absorber layer plays a prominent role in bolstering the PV device performance from <1% to 15%+ efficiency.

For $CdCl_2$-treated CdSeTe/CdTe absorber based solar cells, a notable increase in the J_{SC} was obtained due to the use of a smaller bandgap CdSeTe material toward the front of the device. The small bandgap absorber material increases light absorption in the longer wavelength region of the spectrum and thus more current can be extracted from the PV device.[1,13] In addition to an improved short-circuit current, alloying Se in the CdTe layer also enhances the Open-Circuit Voltage values in CdSeTe/CdTe PV devices (Figure 2 (a)). Such an improvement in the V_{OC} values has been credited to improved minority carrier lifetimes in the absorber.[1,13,19] Figure 1 (b) shows the current density-voltage diode curves for the best performing devices from each substrate. The best performing untreated CdTe device gave an efficiency of 0.22%, while the $CdCl_2$-treated CdTe device gave an efficiency of 15.27%. The efficiency value further increased to 18.30% for the $CdCl_2$-treated CdSeTe/CdTe

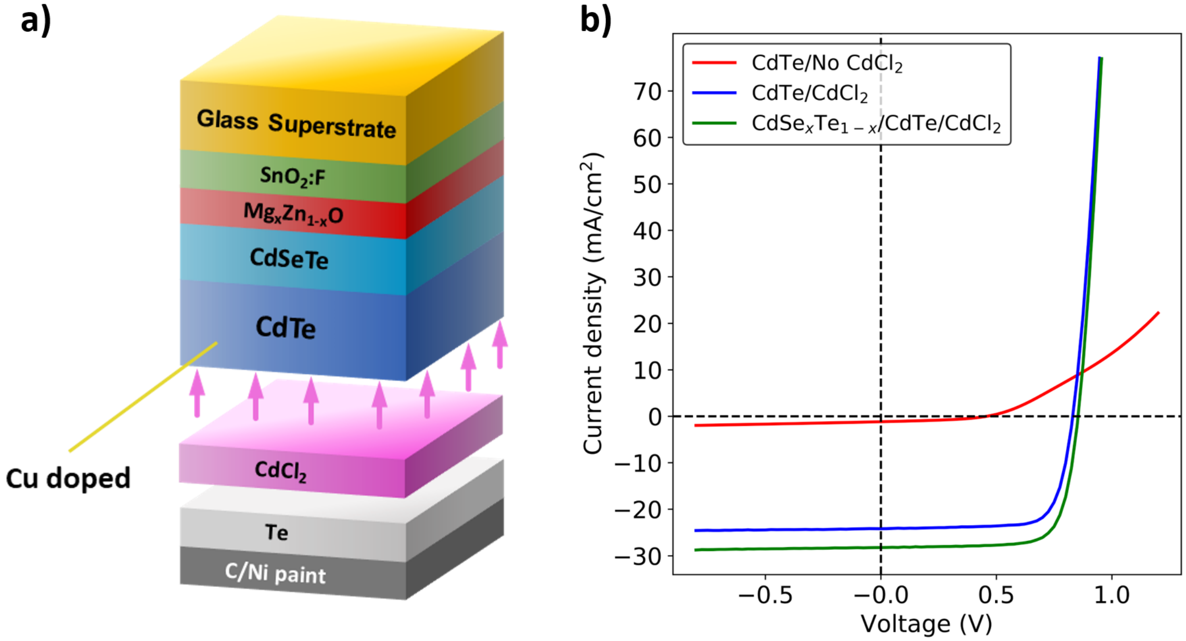

Figure 1: (a) Schematic showing highly efficient CdSeTe/CdTe PV device in superstrate configuration (not to scale). (b) Comparison of the best performing untreated CdTe, $CdCl_2$-treated CdTe and $CdCl_2$-treated CdSeTe/CdTe PV devices.

PV device. Table 1 summarizes the measured device parameters for the above three best performing devices.

Table 1: J-V measurement comparison of the best performing CdTe/No $CdCl_2$, CdTe/$CdCl_2$, and $CdSe_xTe_{1\text{-}x}$/CdTe/$CdCl_2$ PV devices.

Absorber layer	J_{SC} (mA/cm^2)	V_{OC} (mV)	%FF	%η
CdTe/No $CdCl_2$	1.2	460	40.8	0.22
CdTe/$CdCl_2$	24.2	831	76.0	15.27
$CdSe_xTe_{1\text{-}x}$/CdTe/$CdCl_2$	28.3	854	75.8	18.30

To understand the atomic distribution of Se and Cl atoms in the highly efficient $CdCl_2$-treated CdSeTe/CdTe PV device, the elemental mapping was performed using the nano-SIMS technique (described in the methods section) on a similar $CdCl_2$-treated CdSeTe/CdTe absorber film. Figure 3 (a) shows a plane-view image of the chlorine signal intensity in the

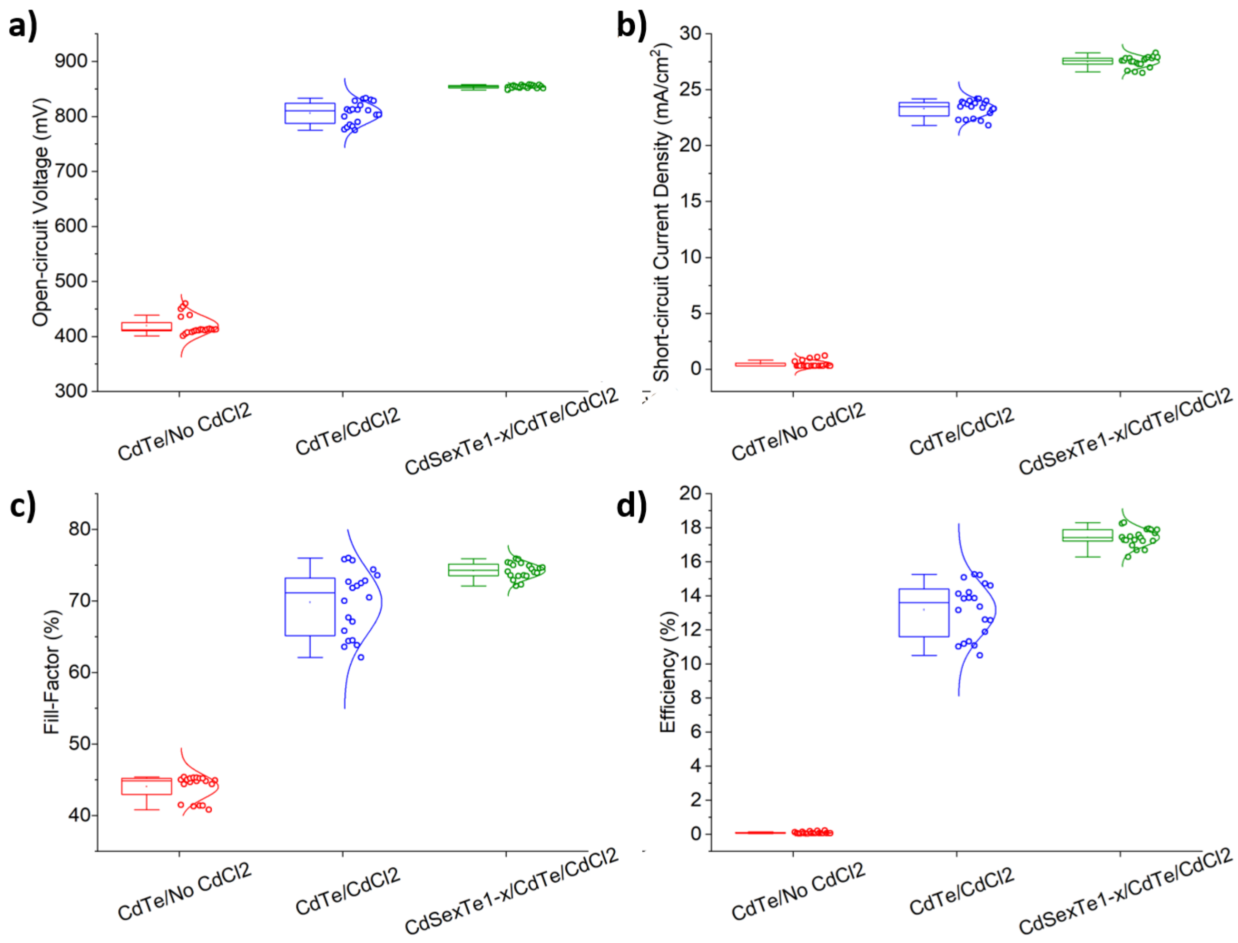

Figure 2: Box plot comparing the (a) Open-Circuit Voltage (V_{OC}) (b) Short-Circuit current density (J_{SC}) (c) Fill Factor (%) (d) Efficiency (η) between untreated CdTe, $CdCl_2$-treated CdTe and $CdCl_2$-treated CdSeTe/CdTe PV devices. Each box plot contains device data for 20 solar cells.

Se-interdiffused CdTe absorber layer. It was observed that the strongest chlorine signal emanates from the CdTe grain boundary regions, with small Cl hotspots located in the interior of the grains. Figure 3 (b) shows a plane-view image of the selenium signal intensity in the CdTe absorber. Apart from being concentrated at the CdTe grain boundaries, selenium signal is also present in the grain fringes. The superimposed image of the chlorine and selenium signals in Figure 3 (c) further confirms that selenium diffuses into the CdTe grains while chlorine is mainly concentrated at the CdTe grain boundary regions. This suggests that during $CdCl_2$ treatment of bilayer CdSeTe/CdTe absorbers Se diffuses into the CdTe grains through the grain boundaries. While analyzing the Se graded CdSeTe/CdTe absorber based PV devices, *Fiducia et al.* and *Guo et al.* have made similar observations in different studies.[14,20] Figure 3 (e) shows a line profile of the selenium and chlorine signals across two grain boundaries in the CdTe absorber layer. As described earlier, the selenium signal was found to be further diffused into the CdTe grain interior compared to chlorine (it should be noted that the chlorine profile will be widened due to the 50-100 nm spot size of the ion beam). Figure 3 (d) shows 3D renderings of the selenium and chlorine signals, showing the diffusion of selenium into the CdTe grains.

Atomistic modeling of CdTe(110)/(100) grain boundary

After determining the Se and Cl distribution in CdTe absorber film, the microstructural mapping of the CdTe film (different from nano-SIMS microscopy) at a random surface (schematic shown in Figure 4 (a)) was done with Electron Back Scatter Diffraction (EBSD) technique. Figure 4 (b) shows the inverse pole image of the $CdCl_2$-treated CdTe film with different colors representing various grain orientations. As evident from Figure 4 (b), the CdTe grains orient themselves in random crystallographic directions forming distinct grain boundary regions. Since EBSD only gives 3 of the 5 macroscopic degrees of freedom that describe the grain boundary, the orientation of the grain boundary plane is random. Using the color code of CdTe grains, one random CdTe(110)/(100) grain boundary (see zoomed view of Figure 4 (b)) was chosen for the atomistic modeling. The basis for choosing CdTe(110)/(100) grain boundary also comes from the previous research study, where *Sen et al.* used Density Functional Theory (DFT) to analyze the electronic properties of CdTe(110)/(100) grain boundary.[21] The atomistic CdTe(110)/(100) model represents an idealistic case of the grain boundary as the twist angle associated with the grain boundary is unknown.

Figure 4 (c) shows the schematic of two probe CdTe(110)/(100) grain boundary model (described in methods section). The interfacial energy per unit area, γ_{GB} was calculated

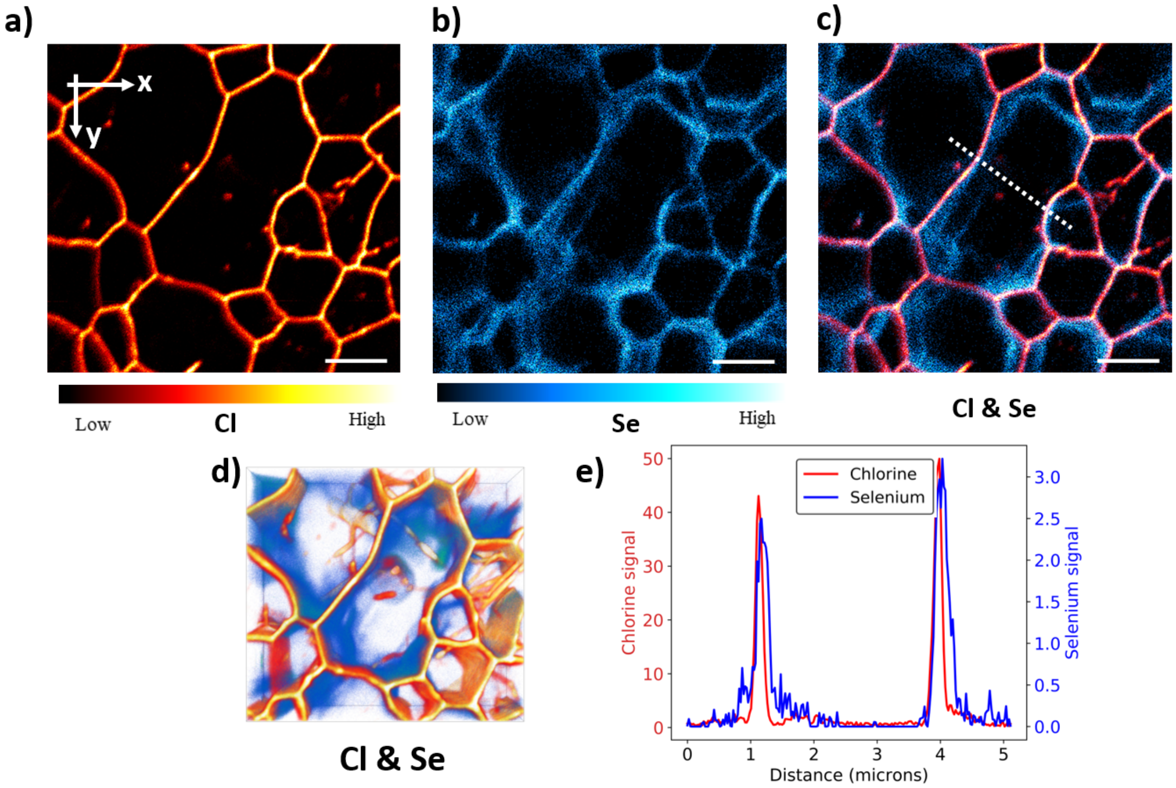

Figure 3: Planar nano-SIMS performed on the $CdCl_2$-treated CdSeTe/CdTe absorber, near the back contact, shows (a) the distribution of Cl along the CdTe grain boundaries (b) the distribution of Se along the CdTe grain boundaries (c) combined distribution of Cl and Se in the absorber. The white dotted line indicates the position of the line profile shown in (f). Scale bars for (a)-(c) are 2μm. (d) 3-D rendering of the chlorine (shown in yellow and red color) and selenium (shown in blue color) distribution in the measurement volume. The x- and y- dimensions of the 3-D renderings are 10 and 9.1 μm, respectively. (e) Line profile of the Cl (red) and Se (blue) signal intensities across the region shown by the dashed line in (c).

from DFT as follows:[22]

$$\gamma_{GB} = \frac{1}{2A}[E^{Total} - E_{bulk,110} \times n_{110} - E_{bulk,100} \times n_{100}] \tag{1}$$

where E^{Total} is defined as the total energy of the grain boundary model, $E_{bulk,110}$ and $E_{bulk,100}$ are the bulk total energies for (110) and (100) orientations respectively, n_{110} and n_{100} are the repeating bulk equivalent unit cells in the respective (110) and (100) orientations that are required to form the central region of the two-probe model, and *'A'* is the cross sectional

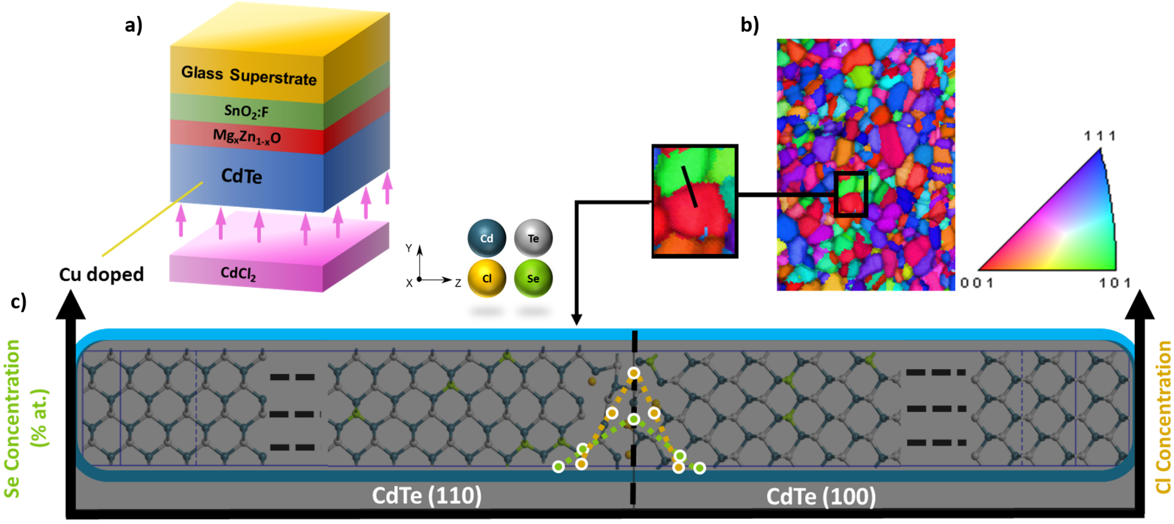

Figure 4: (a) Schematic of $CdCl_2$-treated CdTe absorber film for surface EBSD analysis (b) CdTe surface EBSD image showing various CdTe grain orientations and grain boundaries. The subFigure shows a zoomed view of (110)/(100) CdTe grain boundary chosen for atomistic modeling. (c) Schematic showing a two-probe model of CdTe (110)/(100) grain boundary. The dashed black line indicates the presence of grain boundary. The gold and green line shows the respective Cl and Se atomic concentration distributed across the grain boundary (Figure not drawn to scale). The modeled distribution is the first order approximation of the experimental Se and Cl atomic concentration obtained from nano-SIMS analysis (Figure 3 (e))

area of the simulation domain. The calculated interfacial energy value came out to be 1.37 J/m^2 and is in good agreement with published literature values.[21,22]

For the Se and Cl alloyed CdTe grain boundaries, the interfacial energy γ_{GB} using the two probe model was found to be $\sim$ -730 J/m^2. While the magnitude of the energy was unreasonably lower than the typical grain boundary energy value, a negative sign would suggest that Cl and Se diffusion is favorable at the CdTe grain boundary. The lower magnitude of the interfacial energy could be attributed to the current two probe modeling setup, where the (110) and (110) repeating bulk unit cells constitute only of the Cd and Te atoms. Since Se and Cl atoms are missing from the bulk unit cell, the calculated energy values comes out to be much lower than expected energy values. Nonetheless, the interfacial energy for the Se + Cl alloyed CdTe grain boundary still indicates the segregation of Se and Cl atoms is favorable at the CdTe grain boundaries and can be verified from the nano-SIMS (see Figure 3) results and other published literature.[12,14]

It has been shown earlier by *Li et al.* that the $CdCl_2$ treatment of CdTe absorber leads to substitution of chlorine in the tellurium sites.[12] *Munshi et al., Fiducia et al., and Guo et al.* have also reported that selenium from CdSeTe layer grades into the CdTe absorber by substituting the tellurium sites.[1,13,14] *Guo et al.* using electron energy loss spectroscopy (EELS) further analyzed a similar CdSeTe/CdTe device to arrive to the conclusion that ∼35 at.% Cl and ∼20 at.% Se substitutes the Te sites in the grain boundaries near the CdSeTe/CdTe interface.[14] Based on the atomic distribution of elemental Se and Cl atoms imaged through the nano-SIMS (Figure 3) technique and the literature reports described above, Se and Cl atoms were substituted randomly at the Te sites in the CdTe grain boundary atomistic model. In line with experimental observations, Figure 4 (c) shows a first-order representation of the atomic distribution with the green dashed line representing the diffused Se atoms (maximum concentration ∼20 at.%) and the gold dashed line representing the concentrated Cl atoms (maximum concentration ∼35 at.%) in the two probe CdTe(110)/(100) grain boundary model. However, it is to be noted here that unlike aberration corrected Transmission Electron Microscopy analysis, nano-SIMS imaging does not give the atomic configurations of the atoms at the grain boundaries. Therefore, as mentioned before, the current study utilized other literature reports for determining the Se and Cl atomic configurations in the two probe atomistic models.[12,14]

Pertinent electronic features of the CdTe(110)/(100) atomistic model were studied to understand the copassivation mechanism of alloying Se and Cl atoms in the CdTe grain boundaries. The energy band alignment plot for the bulk CdTe, bare CdTe grain boundary and Se/ Cl alloyed CdTe grain boundary were generated by computing the local density of states and projecting them along the z-direction. Figure 5 and 6 shows the energy band alignment diagrams with macroscopically averaged curve fit of the valence band maximum (VBM) and conduction band minimum (CBM) calculated using the gaussian kernel method described by *Nicholson et al.*[23] The band gap energy, $\mathrm{E}^{\mathrm{g}}_{110}$ and $\mathrm{E}^{\mathrm{g}}_{100}$ were obtained from the energy differences of the CBM and VBM at positions located closest to the bulk CdTe(110) and CdTe(100) electrode ends respectively (Figure 6 (a)). The energy band alignment diagram further shows various features such as a pickup/ dip in the CBM and pickup/ dip in the VBM. As per the labels provided in Figure 5 (b), the peak energy potential in the CBM, $\mathrm{E}_{\mathrm{peak}}$ is defined as the energy difference between the peak curve fit of CBM (labeled point 2) and the curve fit CBM value of the bulk-like CdTe(110) (labeled point 1). A positive value of $\mathrm{E}_{\mathrm{peak}}$ indicates a pickup (barrier for electron charge carriers) while a negative value suggests a dip (enhancer for electron charge carriers) in the CBM at the CdTe(110)/(100) grain boundary. Similarly, cusp energy potential $\mathrm{E}_{\mathrm{cusp}}$ is defined as the energy difference between the peak value of VBM (labeled point 4) and the VBM value of the bulk-like CdTe(110) (labeled point 3). The dip energy potential $\mathrm{E}_{\mathrm{dip}}$ is defined as the energy difference between the lowest dip value of the VBM (labeled point 5) and the VBM value of the CdTe(110) bulk-like region (labeled point 3). The presence of a dip in the VBM indicates an inversion from bulk p-type to n-type at the grain boundary and would act as a barrier for the hole charge carrier transport across the grain boundary. Table 2 summarizes all the electronic features for various grain boundary cases described earlier. A small difference between the band gap values was observed for the bulk-like CdTe(110) and CdTe(100) regions. This difference is majorly due to the screening length which can be accommodated by increasing the number of atoms in the simulation. Nonetheless, the band gap values calculated with DFT-1/2 for the bulk-like CdTe ($\mathrm{E}^{\mathrm{g}}_{110}$ and $\mathrm{E}^{\mathrm{g}}_{100}$) far away from the grain boundary is in good agreement with the existing literature.[22,23]

Classification of the defect states

Figure 5 (a) and (b) shows the energy band alignment features of the bulk CdTe and bare CdTe(110)/(100) grain boundary respectively. Figure 5 (c) and (d) shows the partial charge distribution (obtained by a Mulliken population analysis[24]) on the Cd and Te atoms along

Table 2: Salient electronic features in the energy band alignment of various CdTe(110)/(100) grain boundaries.

CdTe(110)/(100) grain boundary	E^g_{110} (eV)	E^g_{100} (eV)	E_{peak} (eV)	E_{cusp} (eV)	E_{dip} (eV)
Bare	1.44	1.51	0.18	0.66	-0.33
Cl_{Te}	1.51	1.49	-0.64	-	-0.52
Se_{Te}	1.50	1.48	-0.05	0.30	-0.37
Se_{Te} + Cl_{Te}	1.51	1.48	-0.56	-	-0.58

the transverse z-direction for the respective bulk CdTe and CdTe(110)/(100) grain boundary models. Cationic behavior is indicated by a positive electronic charge, while anionic behavior is depicted by a negative electronic charge on the atoms. Figure 5 (c) shows a smooth charge distribution for the bulk CdTe, as the anions and cations are arranged periodically with no perturbation in the electrostatic potential. This unperturbed electrostatic potential manifests itself into a defect state free flat energy band alignment diagram with energy bandgap value of ∼1.51 eV throughout the bulk CdTe model.

However, the atoms at the CdTe(110)/(100) grain boundary deviates from the ordered anionic/cationic arrangement. The deviation from periodic arrangement of atoms induces a perturbation in the electrostatic potential and therefore affect the charges on the atoms (see Figure 5 (d)) near the grain boundary region. Such a disordered arrangement of atoms with varying degree of charge near the grain boundary creates electronic defect states in the bandgap region. These defect states can be further classified into donor or acceptor states. A donor defect state is defined as the state which donates electrons to the CBM and in turn becomes positively charged while the acceptor states accepts electrons from the VBM, thereby becoming negatively charged states. Figure 7 shows the density of defect states for the bare and alloyed CdTe(110)/(100) grain boundary cases. The quantified density of defect states is quantitatively in good agreement with other published literature.[25] The presence of the defect states (shallow or deep levels) bend the bands depending on whether they are acceptor or donor defect states.

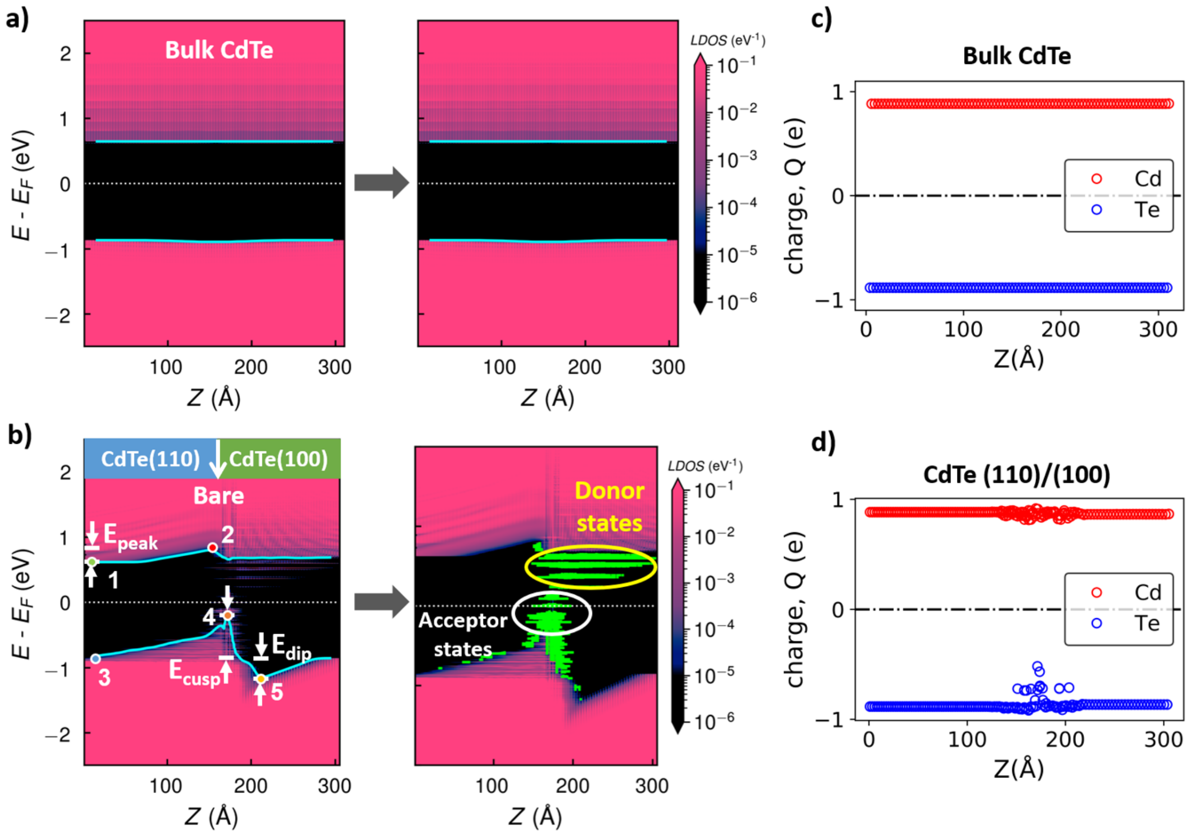

Figure 5: Energy band alignment diagram of the (a) bulk CdTe and (b) CdTe (110)/(100) grain boundary. The top arrow indicates the grain boundary plane. The white dotted line denotes the Fermi energy level and the blue curves are the macroscopic average fits of the VBM and CBM. The second set of energy band alignment diagrams highlights the grain boundary defect states (indicated by green lines) mapped with respect to energy and localized positions based on 10^{-5}/eV Local Density of States (LDOS) cutoff value. Mulliken population analysis shows the atomic charge distribution for (c) bulk CdTe and (d) CdTe (110)/(100) grain boundary.

Therefore, it is important to understand the character of the defect states to comprehend the various electronic features observed in the energy band alignment diagram of bare/alloyed CdTe(110)/(100) grain boundaries. Based on 10^{-5}/eV LDOS cutoff value, existing defect states (indicated by green lines in Figure 5 (b)) were algorithmically determined with respect to energy and localized position (in transverse z-direction) in the energy band alignment diagrams. Since the origin of these sub bandgap defect states is due to variation in the atomic charges, it was theorized that the characteristics of these defect states could be

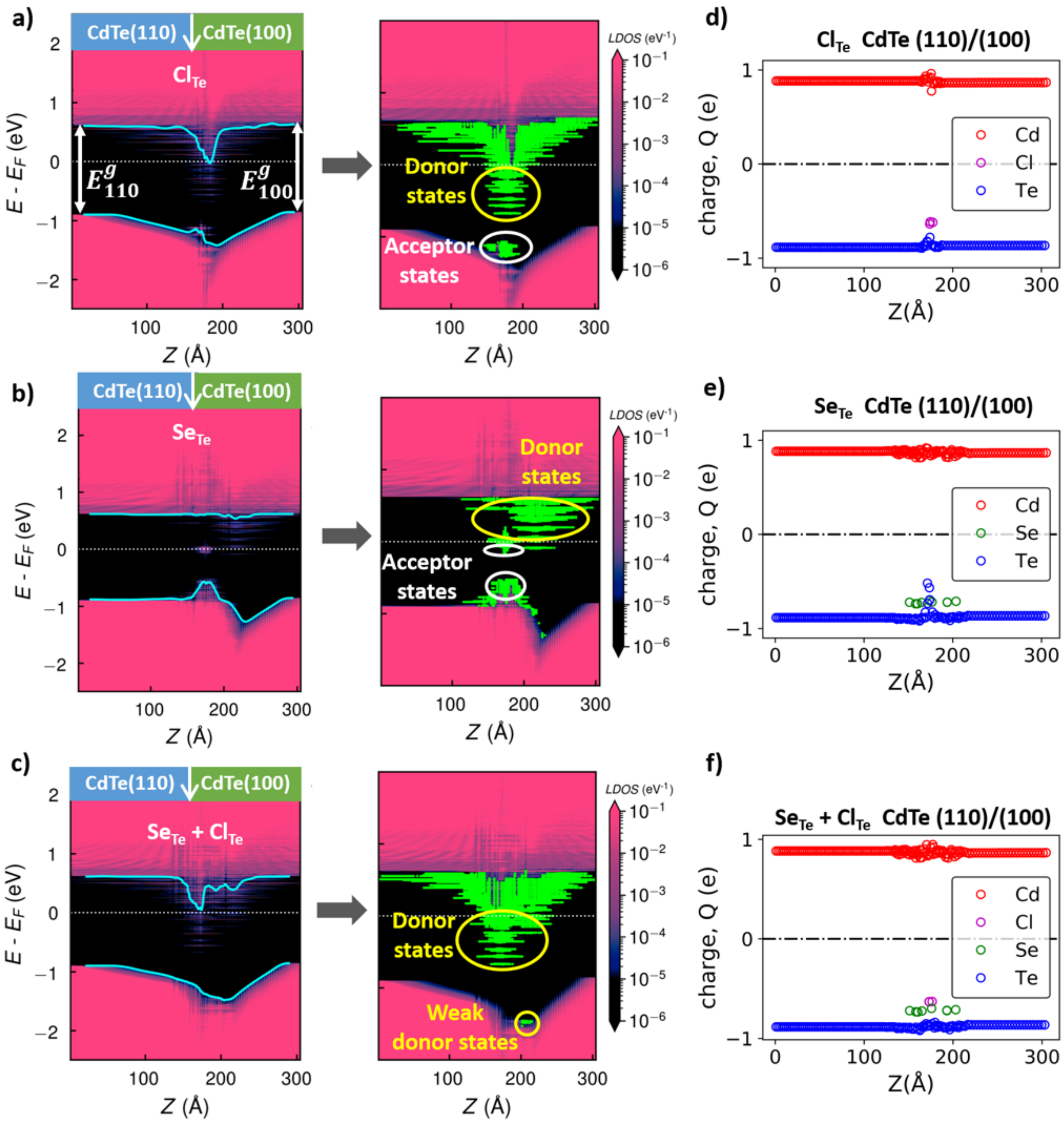

Figure 6: Energy band alignment diagram of the (a) Cl_{Te} CdTe (110)/(100) grain boundary (b) Se_{Te} CdTe (110)/(100) grain boundary and (c) Se_{Te} + Cl_{Te} CdTe (110)/(100) grain boundary along with their respective mapped defect states based on 10^{-5}/eV LDOS cutoff value. The top arrow indicates the grain boundary plane. Mulliken population analysis further shows the atomic charge distribution for (d) Cl_{Te} CdTe (110)/(100) grain boundary (e) Se_{Te} CdTe (110)/(100) grain boundary and (f) Se_{Te} + Cl_{Te} CdTe (110)/(100) grain boundary.

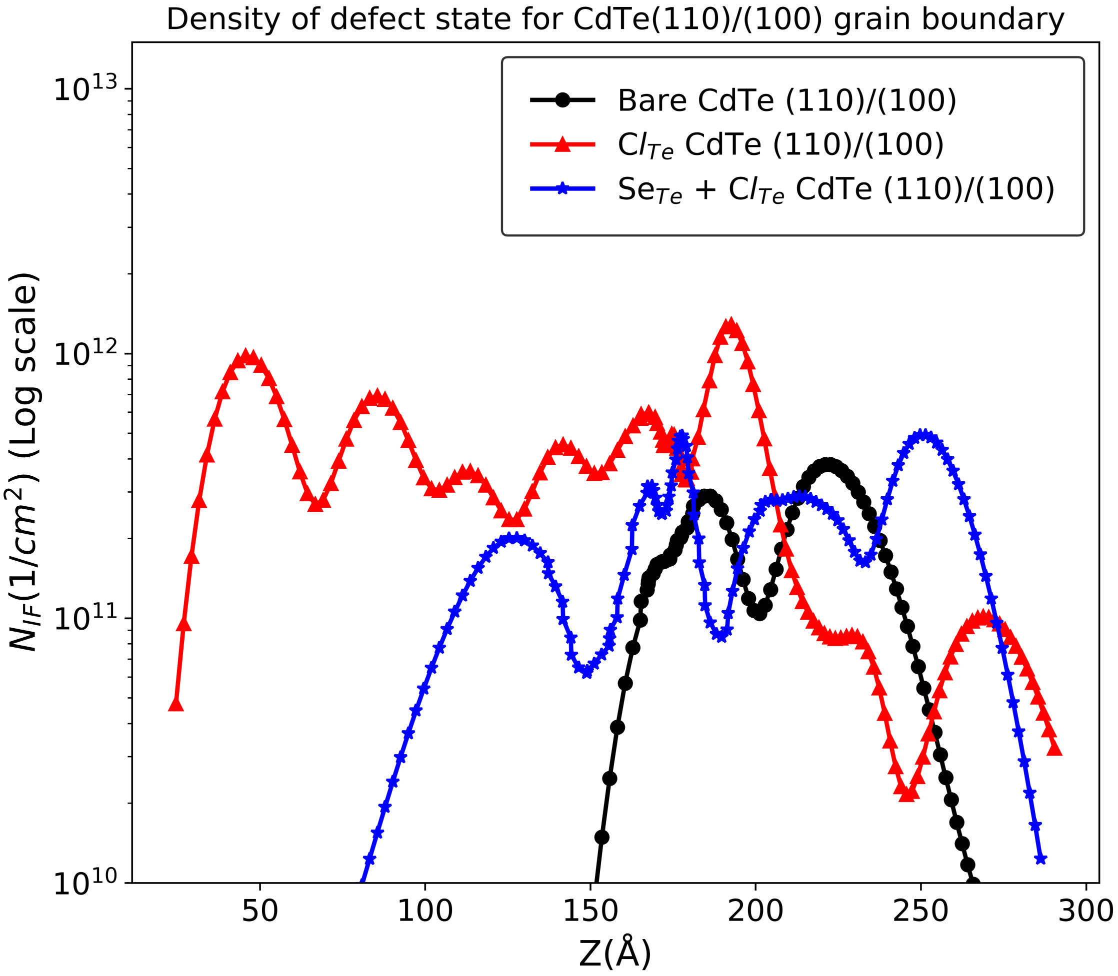

Figure 7: Density of defect state with respect to the transverse z-direction for bare, $\mathrm{Cl_{Te}}$, and $\mathrm{Se_{Te}}$ + $\mathrm{Cl_{Te}}$ alloyed CdTe (110)/(100) grain boundary.

directly determined by summing the charges on the atoms contributing to the existence of these defect states. If the net charge on atoms contributing to a particular defect state was found to be positive/negative, that state would be classified as a donor/acceptor state.

In regards to this, clusters of the defect states existing near different energy band alignment features were identified and the ones having highest LDOS value were analyzed to determine their respective character. For example, for the bare CdTe(110)/(100) grain boundary in Figure 5 (b), two groups of defect states near the $\mathrm{E_{cusp}}$ and $\mathrm{E_{dip}}$ energy potentials were identified. From the defect state group near the $\mathrm{E_{cusp}}$ energy potential, two defect states with highest LDOS values at $E_{defect1} = -0.118$ eV (LDOS $= 0.17136$ eV^{-1}) and $E_{defect2} = 0$ eV (LDOS $= 0.02385$ eV^{-1}) were selected for further analysis. Using the data generated after mapping the localized positions of the defect states, $E_{defect1}$ extended from $z_{\text{start}} = 144.11$ Å to $z_{\text{end}} = 187.92$ Å in the transverse z-direction. Using the Mulliken population plot in Figure 5 (d), it was found that a total of 74 atoms with a net -1.27 electronic charge was associated with $E_{defect1}$ across the specified spatial range. Likewise, defect state 2 ($E_{defect2} = 0$ eV) was located from $z_{\text{start}} = 148.80$ Å to $z_{\text{end}} = 196.21$ Å with a total of 88 atoms having a net -1.26 electronic charge contributing to its existence. Since, the net electronic charge on the atoms contributing to the defect state 1 and defect state 2 were negative, both of these defect states were classified as acceptor states.

Similarly, from the other group of defect states above the E_{dip} energy potential, two defect states with highest LDOS value at $E_{defect3} = 0.362$ eV (LDOS $= 0.05402$ eV^{-1}) and $E_{defect4} = 0.531$ eV (LDOS $= 0.69080$ eV^{-1}) were analyzed. Defect state 3 ($E_{defect3} = 0.362$ eV) was located from $z_{\text{start}} = 155.83$ Å to $z_{\text{end}} = 255.86$ Å with a total of 180 atoms having a net +0.45 electronic charge. Likewise, defect state 4 ($E_{defect4} = 0.531$ eV) was located from $z_{\text{start}} = 148.80$ Å to $z_{\text{end}} = 298.94$ Å with a total of 272 atoms having a net +1.33 electronic charge. Since, the net electronic charge on the atoms contributing to the defect state 3 and defect state 4 were positive, these defect states were classified as donor states. Table 3 summarizes the analysis of various defect states for bare CdTe(110)/(100) grain boundary. Based on the above analysis, it could be deduced that the cluster of defect states above the E_{cusp} energy potential would be acceptor states (labeled with white circle in Figure 5 (b)) and the ones above the E_{dip} energy potential would be donor states (labeled with yellow circle in Figure 5 (b)). Furthermore, these donor and acceptor states were classified as deep level defect states as they were found in the mid bandgap region for the bare CdTe grain boundary model.

To understand the effect of alloying elements on the defect states, similar analyses were performed on the Se and Cl alloyed CdTe(110)/(100) grain boundary models. It was observed that the presence of Cl_{Te} at the grain boundary leads to emergence of high density of deep level donor states (see Figure 6 (a)) below the Fermi level. However, acceptor type defect states were found near the VBM indicating the presence of shallow level acceptor states. This implies that passivating the grain boundaries with $\mathrm{Cl_{Te}}$ eliminates the deep level acceptor defect states (found in the bare grain boundary) but introduces high density of deep level donor states.

The defect state analysis for $\mathrm{Se_{Te}}$ alloyed CdTe grain boundary indicated a lower deep level acceptor state density (see Figure 6 (b)) than the bare CdTe grain boundary case. In addition to that, the high density of both shallow and deep level donor states were found to exist above the Fermi level. However, alloying the grain boundary with $\mathrm{Se_{Te}} + \mathrm{Cl_{Te}}$ revealed the exclusive presence of donor defect states. The model indicates that $\mathrm{Se_{Te}} + \mathrm{Cl_{Te}}$ completely passivates the acceptor defects present in either of the bare, $\mathrm{Cl_{Te}}$ or $\mathrm{Se_{Te}}$ alloyed CdTe grain boundaries (see Figure 6 (c)). Table 3 summarizes the analysis of various defect states for the alloyed CdTe(110)/(100) grain boundary.

It is also important to note here that this work doesn't attempt to relate Mulliken population charge to the defect charge rather utilizes Mulliken population charge to identify the nature of defect states. Mulliken population charge on atoms consists of complex interactions between the electronic wavefunctions that forms defect states with different defect charge values. Therefore, establishing a relationship between the Mulliken population charge to the defect charge is complicated and is beyond the scope of the current work.

Effect of defect states on the energy band alignment diagram

As described before, the presence of defect states have certain implications on the energy band alignment diagrams. Previous literature reports have shown that high density of donor/acceptor states creates a dip/cusp energy potential in the VBM.[25,26] Similar effects were observed in the bare and alloyed CdTe grain boundaries. It was consistently found that the presence of donor defect states begin near the CBM and extends down toward the mid bandgap region. This would facilitate the donation of minority electron charge carriers to

Table 3: Summary of the analysis of defect states for the bare and alloyed CdTe(110)/(100) grain boundary.

Alloy	E_{defect} (eV)	LDOS (eV^{-1})	z_{start} (Å)	z_{end} (Å)	N_{atoms}	M.P. charge (e-)	Defect State
Bare	-0.118	0.17136	144.11	187.92	74	-1.27	Acceptor
	0	0.02385	148.80	196.21	88	-1.26	Acceptor
	+0.362	0.05402	155.83	255.86	180	+0.45	Donor
	+0.531	0.69080	148.80	298.94	272	+1.33	Donor
Cl_{Te}	-1.25	0.01599	167.82	187.69	25	-0.38	Acceptor
	-1.23	0.12646	169.60	194.32	45	-0.40	Acceptor
	-1.11	0.14756	146.46	191.00	80	-1.26	Acceptor
	-0.293	0.32214	148.80	205.91	103	+1.32	Donor
Se_{Te}	-0.768	0.23196	137.16	205.32	120	-1.24	Acceptor
	-0.056	0.03154	162.52	186.99	45	-2.21	Acceptor
	+0.037	0.21187	151.17	245.50	171	+1.38	Donor
	+0.55	1.40320	185.32	262.07	140	+2.59	Donor
Se_{Te} + Cl_{Te}	-1.46	0.00033	201.66	214.99	23	+0.009	Weak Donor
	-0.356	0.37712	141.76	202.98	108	+0.556	Donor
	-0.068	0.01023	148.88	189.75	73	+1.41	Donor
	+0.181	1.57267	137.16	228.24	164	+0.44	Donor

the CBM by the donor states and would make them positively charged. The presence of positively charged donor defect states in the bandgap region would further cause a repulsive field for hole charge carriers and create a barrier (dip energy potential) in the VBM. This further explains the existence of donor defect states above the E_{dip} energy potential in the bare and alloyed CdTe grain boundaries (Figure 5 and 6).

Similarly, the acceptor states begin near the VBM and protude into the bandgap region. The shallower acceptor states would gain an electron from the VBM and create hole charge carriers. This would generate an attractive electric field for the hole charge carriers and bends the VBM up toward the acceptor defect states leading to formation of cusp electric potentials (E_{cusp}) in the VBM. Such a trend was observed in all the grain boundary cases where acceptor states were found to exist above the VBM (see Figure 5 (b) and 6 (b)). For the Cl alloyed CdTe grain boundary (Figure 6 (a)), since the density of acceptor was not high, a small cusp like feature in the VBM near the acceptor states was observed instead of a high energy cusp potential. This further confirms the fact that, however small but VBM always bends up in the vicinity of the acceptor states and bends down in vicinity of the donor states. A similar conclusion is found for how donor/ acceptor states influence the band bending direction in the CBM. Such an approach to understand the impact of defect states on the energy band alignment behavior reinforces the Mulliken population analysis results that were used to characterize the defect states.

Discussion

The atomistic modeling of the bare and alloyed CdTe(110)/(100) grain boundary gives insight into the effect of the selenium and chlorine elements on the grain boundary electronic properties. The electronic properties of the bare, Cl_{Te}, and Se_{Te} + Cl_{Te} alloyed CdTe grain boundary models could provide major insights into the performance of the untreated CdTe, $CdCl_2$-treated CdTe, and $CdCl_2$-treated CdSeTe/CdTe PV devices. It is a known fact that occupation probability of a defect state depends on its energy position (E_{def}) relative to the Fermi level (E_f). It has been shown previously that the occupation probability of a defect state ($P(E_{def}$ - $E_f)$) could be determined as:[26]

$$P(E_{\mathrm{def}} - E_{\mathrm{f}}) = 1, E_{\mathrm{def}} < E_{\mathrm{f}} \tag{2}$$

$$P(E_{\mathrm{def}} - E_{\mathrm{f}}) = 0, E_{\mathrm{def}} > E_{\mathrm{f}} \tag{3}$$

In regards to the defect states, equation 2 and equation 3 states that donor(acceptor) state above(below) the Fermi level contain positive(negative) charge.[25] As has been discussed before, for the bare CdTe grain boundary case (Figure 5 (b)), the donor states above the Fermi level will be positively charged while the acceptor states will be negatively charged. Moreover, these states are in the close vicinity and therefore have a high probability of charge carrier recombination. Apart from that, a positive E_{peak} value (see table 2) in the CBM creates an electron reflector type effect and E_{dip} (see table 2) energy potential in the VBM creates a barrier for hole charge carriers. Therefore, the high probability of charge recombination at the grain boundary and transport barrier of the minority electron charge carriers (assuming p-type CdTe absorber) at the grain boundary should limit the device performance of untreated CdTe solar cells.

However, as described before, the Cl_{Te} alloying of the CdTe grain boundary passivates the deep level acceptor states but induces high density of donor states. In one of the literature report, *Mhirech et al.* showed that the existence of high density donor states leads to an inversion at the interface and is beneficial for extracting the minority charge carriers.[26] Similar effects were observed for the Cl_{Te} alloyed CdTe grain boundary in this study. The presence of high density of donor states leads to a negative E_{peak} energy potential in the CBM and a high E_{dip} energy potential in the VBM (see table 2). This implies that both the CBM and VBM bend downwards causing an n-type inversion (from a p-type grain interior) at the grain boundary. Due to this inversion, minority electron charge carriers would be attracted toward the grain boundary while majority charge carriers would be repelled, leading to better charge carrier extraction. Moreover, the presence of shallower acceptor defect states further reduces the recombination in the Cl_{Te} alloyed CdTe grain boundary. Such low recombination and a better minority charge carrier collection in the $CdCl_2$-treated CdTe PV devices should improve the open circuit voltage and short-circuit current density as observed in Figure 2.

The Se_{Te} + Cl_{Te} alloying of CdTe grain boundary passivates both the deep and shallow level acceptor states found in the respective bare and Cl_{Te} alloyed of CdTe grain boundary. The high density of donor states maintains the inversion at the grain boundary, again allowing for a better minority electron charge carrier collection. This would further reduce the charge recombination (compared to the $\mathrm{Cl_{Te}}$ alloyed CdTe grain boundary) and increase the minority charge carrier lifetime for CdSeTe/CdTe PV devices. In past, *Guo et al.* has made similar observations, where minority carrier lifetime of 6.3 ns was measured for the $\mathrm{Se_{Te}} + \mathrm{Cl_{Te}}$ alloyed CdTe absorber in comparison to 1 ns lifetime obtained for the pure CdTe layer.[14] The low charge carrier recombination and improved minority charge carrier lifetime should further promote higher open circuit voltages in $\mathrm{CdCl_2}$-treated CdSeTe/CdTe PV devices (see Figure 2 (a)). The presence of the lower bandgap CdSeTe material also leads to higher short-circuit current values (see Figure 2 (b)), thereby improving the PV device efficiencies beyond 18%.

It is important to note that the overall efficiency improvements due to $\mathrm{Se_{Te}} + \mathrm{Cl_{Te}}$ alloying of CdTe absorber would also depend on the potentials created due to other grain boundary defects, grain size, interfaces created due to various front and back contacts, and bulk properties of the absorber. *Li et al.* in previous study showed that electrostatic field created due to the presence of $\mathrm{Cl_{Te}}$ leads to n-type inversion and could be generalized for any random CdTe grain boundary.[12] Although, this is expected to hold true with respect to the energy band alignment results, a detailed systematic study is required to understand the passivating effect of $\mathrm{Se_{Te}} + \mathrm{Cl_{Te}}$ atoms on the symmetric and random CdTe grain boundary orientation. Such an investigation using the methodologies presented in the current study would lead to a set of quantified defect parameters for various CdTe grain boundaries. These quantified defect parameters for diverse grain boundaries could be further utilized in 2D/3D device models to validate the experimental performance. Overall, the current study provides useful insights into the quantification and nature of the defect states, whose understanding could further enhance the performance of the CdTe solar cells.

Conclusion

In summary, we compare the device performance parameters of the untreated CdTe, $CdCl_2$-treated CdTe, and $CdCl_2$-treated CdSeTe/CdTe PV devices. Nano-SIMS characterization of highly efficient CdSeTe/CdTe devices reveals the elemental distribution of the selenium and chlorine atoms. While chlorine was found to be concentrated in the CdTe grain boundaries, selenium atoms were found to diffuse into CdTe grains via the grain boundary regions. The surface EBSD analysis of the CdTe film showed various grain orientations forming distinct grain boundary regions from which a random CdTe(110)/(100) grain boundary was chosen for the atomistic modeling. Various CdTe(110)/(100) grain boundary models including the bare, Cl_{Te}, and Se_{Te} + Cl_{Te} alloyed CdTe grain boundary were simulated. The energy band alignment and the defect state properties evaluated using DFT calculations aids in deducing the mechanism for highly efficient CdSeTe/CdTe absorber based PV devices. The presence of selenium and chlorine alloying atoms passivates the acceptor level defect states and induces high density of donor states. The passivation of acceptor defect states reduces the recombination while the high density donor states leads to n-type inversion at the grain boundary. The inversion from p-type grain interior to n-type grain boundary enhances the minority charge carrier collection, leading to a higher open-circuit voltage and short-circuit current density observed in highly efficient CdSeTe/CdTe PV devices.

Methods

Cell fabrication and nano-SIMS characterization Photovoltaic devices with two CdTe and one CdSeTe/CdTe p-type absorbers were fabricated using an in-line sublimation system described by *Swanson et al.*[27] 20 small area ∼ 0.65 cm^2 research devices were fabricated on NSG Pilkington TEC10 soda lime glass using the methods described by *Munshit et al.*[1,2] The electrical measurements were performed after calibrating the Current-density and device area for each set of measurement to cells measured by National Renewable Energy

Laboratory (NREL). For the nano-SIMS characterization, a region of the back surface of the absorber layer (i.e. in the CdTe part of the absorber, near the back contact) was first polished with a Xe ion beam to remove surface roughness and prepare the samples for SIMS measurements. NanoSIMS measurements were then performed on the polished region using the methods described by *Fiducia et al.*[20]

Computational details CdTe(110)/(100) grain boundary model was simulated using the QuantumATK P-2019.03 software tool.[28] The pseudopotential, basis sets and other modeling parameters for Cd, Se, Te and Cl atoms were chosen from the earlier studies performed by *Shah et al.*[15,22] All the simulation utilized Perdew-Zunger form of Local Density Approximation (LDA-1/2)[29] exchange correlation functional for the self-consistent calculations[30] with 6x6x150 k-point sampling for CdTe grain boundary two-probe device simulations (schematic shown in Figure 4 (c)).

Acknowledgement

The material is partially based upon work supported by the U.S. Department of Energy's Office of Energy Efficiency and Renewable Energy (EERE) under Solar Energy Technologies Office (SETO) Agreement number DE-EE0008557 and DE-EE0008177. Acknowledgment goes out to the National Science Foundation Graduate Research Fellowship, INTERN, and NSF/IUCRC Programs for the support and funding of the current research work. This work utilized the Summit supercomputer, which is supported by the National Science Foundation (awards ACI-1532235 and ACI-1532236), the University of Colorado Boulder, and Colorado State University. J. Liu and C. Grovenor are grateful for support for the NanoSIMS facility from EPSRC under grant EP/M018237/1.

Disclaimer

This report was prepared as an account of work sponsored by an agency of the United States Government. Neither the United States Government nor any agency thereof, nor any of their employees, makes any warranty, express or implied, or assumes any legal liability or responsibility for the accuracy, completeness, or usefulness of any information, apparatus, product, or process disclosed, or represents that its use would not infringe privately owned rights. Reference herein to any specific commercial product, process, or service by trade name, trademark, manufacturer, or otherwise does not necessarily constitute or imply its endorsement, recommendation, or favoring by the United States Government or any agency thereof. The views and opinions of authors expressed herein do not necessarily state or reflect those of the United States Government or any agency thereof.

References

(1) Munshi, A. H.; Kephart, J.; Abbas, A.; Raguse, J.; Beaudry, J.; Barth, K.; Sites, J.; Walls, J.; Sampath, W. Polycrystalline CdSeTe/CdTe Absorber Cells with 28 mA/cm2 Short-Circuit Current. *IEEE Journal of Photovoltaics* **2018**, *8*, 310–314.

(2) Munshi, A. H.; Kephart, J. M.; Abbas, A.; Shimpi, T. M.; Barth, K. L.; Walls, J. M.; Sampath, W. S. Polycrystalline CdTe Photovoltaics with Efficiency Over 18% through Improved Absorber Passivation and Current Collection. *Solar Energy Materials and Solar Cells* **2018**, *176*, 9 – 18.

(3) Kephart, J. M.; Kindvall, A.; Williams, D.; Kuciauskas, D.; Dippo, P.; Munshi, A.; Sampath, W. S. Sputter-Deposited Oxides for Interface Passivation of CdTe Photovoltaics. *IEEE Journal of Photovoltaics* **2018**, *8*, 587–593.

(4) Hagenorf, C. *Assessment of Performance, Environmental, Health and Safety Aspects of First Solar's CdTe Photovoltaic Technology*; 2016.

(5) Bosio, A.; Romeo, N.; Podestà, A.; Mazzamuto, S.; Canevari, V. Why CuInGaSe2 and CdTe Polycrystalline Thin Film Solar Cells are More Efficient than the Corresponding Single Crystal? *Crystal Research and Technology* **2005**, *40*, 1048–1053.

(6) Dharmadasa, I. M. Review of the CdCl2 Treatment Used in CdS/CdTe Thin Film Solar Cell Development and New Evidence towards Improved Understanding. *Coatings* **2014**, *4*, 282–307.

(7) Paulson, P.; Dutta, V. Study of In Situ CdCl2 Treatment on CSS Deposited CdTe Films and CdS/CdTe Solar Cells. *Thin Solid Films* **2000**, *370*, 299 – 306.

(8) Schaffner, J.; Motzko, M.; Tueschen, A.; Swirschuk, A.; Schimper, H.-J.; Klein, A.; Modes, T.; Zywitzki, O.; Jaegermann, W. 12% Efficient CdTe/CdS Thin Film Solar Cells Deposited by Low-Temperature Close Space Sublimation. *Journal of Applied Physics* **2011**, *110*, 064508.

(9) Kim, M.; Sohn, S.; Lee, S. Reaction Kinetics Study of CdTe Thin Films During CdCl2 Heat Treatment. *Solar Energy Materials and Solar Cells* **2011**, *95*, 2295 – 2301, Photovoltaics, Solar Energy Materials Thin Films, IMRC 2009-Cancun.

(10) Moutinho, H. R.; Al-Jassim, M. M.; Levi, D. H.; Dippo, P. C.; Kazmerski, L. L. Effects of CdCl2 Treatment on the Recrystallization and Electro-Optical Properties of CdTe Thin Films. *Journal of Vacuum Science & Technology A* **1998**, *16*, 1251–1257.

(11) Zhang, L.; Da Silva, J. L. F.; Li, J.; Yan, Y.; Gessert, T. A.; Wei, S.-H. Effect of Copassivation of Cl and Cu on CdTe Grain Boundaries. *Phys. Rev. Lett.* **2008**, *101*, 155501.

(12) Li, C.; Wu, Y.; Poplawsky, J.; Pennycook, T. J.; Paudel, N.; Yin, W.; Haigh, S. J.; Oxley, M. P.; Lupini, A. R.; Al-Jassim, M.; Pennycook, S. J.; Yan, Y. Grain-Boundary-Enhanced Carrier Collection in CdTe Solar Cells. *Phys. Rev. Lett.* **2014**, *112*, 156103.

(13) Fiducia, T. A.; Mendis, B. G.; Li, K.; Grovenor, C. R.; Munshi, A. H.; Barth, K.; Sampath, W. S.; Wright, L. D.; Abbas, A.; Bowers, J. W.; Walls, J. M. Understanding the Role of Selenium in Defect Passivation for Highly Efficient Selenium-Alloyed Cadmium Telluride Solar Cells. *Nature Energy* **2019**, *4*, 504–511.

(14) Guo, J.; Mannodi-Kanakkithodi, A.; Sen, F. G.; Schwenker, E.; Barnard, E. S.; Munshi, A.; Sampath, W.; Chan, M. K.; Klie, R. F. Effect of Selenium and Chlorine Co-passivation in Polycrystalline CdSeTe Devices. *Applied Physics Letters* **2019**, *115*.

(15) Shah, A.; Munshi, A. H.; Nicholson, A. P.; Thiyagarajan, A.; Pozzoni, U. M.; Sampath, W. S. Atomistic Modeling of Energy Band Alignment in CdSeTe Surfaces. *Applied Surface Science* **2021**, *544*, 148762.

(16) Watts, M. J.; Fiducia, T. A. M.; Sanyal, B.; Smith, R.; Walls, J. M.; Goddard, P. Enhancement of Photovoltaic Efficiency in CdSe x Te1-x (where 0 x 1): Insights from Density Functional Theory. *Journal of Physics: Condensed Matter* **2019**, *32*, 125702.

(17) Wei, S.-H.; Zhang, S. B.; Zunger, A. First-Principles Calculation of Band Offsets, Optical Bowings, and Defects in CdS, CdSe, CdTe, and their Alloys. *Journal of Applied Physics* **2000**, *87*, 1304–1311.

(18) Swanson, D. E.; Sites, J. R.; Sampath, W. S. Co-Sublimation of CdSexTe1x Layers for CdTe Solar Cells. *Solar Energy Materials and Solar Cells* **2017**, *159*, 389–394.

(19) Kuciauskas, D.; Kephart, J. M.; Moseley, J.; Metzger, W. K.; Sampath, W. S.; Dippo, P. Recombination Velocity Less than 100cm/s at Polycrystalline Al2O3/CdSeTe Interfaces. *Applied Physics Letters* **2018**, *112*, 263901.

(20) Fiducia, T. A. M.; Li, K.; Munshi, A. H.; Barth, K.; Sampath, W. S.; Grovenor, C. R. M.; Walls, J. M. Three-Dimensional Imaging of Selenium and Chlorine Distributions in Highly Efficient Selenium-Graded Cadmium Telluride Solar Cells. *IEEE Journal of Photovoltaics* **2020**, *10*, 685–689.

(21) Sen, F. G.; Buurma, C.; Paulauskas, T.; Ce Sun,; Moon Kim,; Sivananthan, S.; Klie, R. F.; Chan, M. K. Y. Atomistic Simulations of Grain Boundaries in CdTe. 2015 IEEE 42nd Photovoltaic Specialist Conference (PVSC). 2015; pp 1–5.

(22) Shah, A.; Nicholson, A. P.; Thiyagarajan, A.; Sampath, W. S. First Principles Assisted Modeling to Understand Chlorine Passivation of CdTe Grain Boundary. 2020 47th IEEE Photovoltaic Specialists Conference (PVSC). 2020; pp 1760–1764.

(23) Nicholson, A. P.; Martinez, U.; Shah, A.; Thiyagarajan, A.; Sampath, W. S. Atomistic Modeling of Energy Band Alignment in CdTe(1 0 0) and CdTe(1 1 1) Surfaces. *Applied Surface Science* **2020**, *528*, 146832.

(24) Mulliken, R. S. Electronic Population Analysis on LCAO. *J. Chem. Phys* **1955**, *23*, 1833.

(25) Scheer, R.; Schock, H. W. *Chalcogenide Photovoltaics*; John Wiley Sons, Ltd, Chapter 2, pp 9–127.

(26) Mhirech, A.; Baddi, M. *Energy and the Environment*; Pergamon: Oxford, 1990; pp 448–452.

(27) Swanson, D. E.; Kephart, J. M.; Kobyakov, P. S.; Walters, K.; Cameron, K. C.; Barth, K. L.; Sampath, W. S.; Drayton, J.; Sites, J. R.; Kephart, J. M.; Kobyakov, P. S.; Walters, K.; Cameron, K. C.; Barth, K. L.; Sampath, W. S. Single Vacuum Chamber with Multiple Close Space Sublimation Sources to Fabricate CdTe Solar Cells. **2017**, *021202*.

(28) QuantumATK 2019.03, Synopsys QuantumATK.

(29) Ferreira, L. G.; Marques, M.; Teles, L. K. Approximation to Density Functional Theory for the Calculation of Band Gaps of Semiconductors. *Physical Review B - Condensed Matter and Materials Physics* **2008**, *78*, 1–9.

(30) Perdew, J. P.; Ernzerhof, M.; Burke, K. Rationale for Mixing Exact Exchange with Density Functional Approximations. *Journal of Chemical Physics* **1996**, *105*, 9982–9985.

Graphical TOC Entry